Available online at www.sciencedirect.com
ScienceDirect
Trans. Nonferrous Met. Soc. China 34(2024) 786−797
Transactions of Nonferrous Metals Society of China
www.tnmsc.cn

Coordinated deformation behavior and gas bulging formability of hot-pressed Ni/Al micro-laminated composite sheet

Yu-peng LU[1], Hong-liang YIN[1], Xian-zheng XI[1], Ling-jian MENG[1], Peng LIN[1,2], Wei LIANG[1]

1. College of Materials Science and Engineering, Taiyuan University of Technology, Taiyuan 030024, China;
2. Engineering Research Center of Advanced Metal Composites Forming Technology and Equipment of Ministry of Education, Taiyuan University of Technology, Taiyuan 030024, China

Received 11 August 2022; accepted 30 December 2022

Abstract: To fabricate NiAl complex thin-walled components, a novel Ni/Al micro-laminated composite sheet (NAMCS) was prepared by vacuum hot-pressing. Based on the uniaxial tensile tests at different temperatures, the mechanical properties of NAMCS were investigated. To clarify the uniaxial tensile coordinated deformation mechanism of NAMCS, the deformed microstructure at different tensile strains was characterized by scanning electron microscopy. The results showed that some cracks formed in $NiAl_3$ and Ni_2Al_3 layers at a tensile strain of 5%, room temperature and 300 °C. At 600 °C and a tensile strain of 20%, some microvoids were observed in the $NiAl_3$ layers, but no cracks formed in the Ni_2Al_3 layers until the sample fractured at a tensile strain of 78.7%. This indicated a good coordinated deformation ability. The high-temperature free gas bulging test of NAMCS showed that the limit bulging ratio (the ratio of limit bulging height to die diameter) of NAMCS at 600 °C reached 33.3%, implying good formability.

Key words: Ni/Al micro-laminated composite sheet; mechanical properties; coordinated deformation mechanism; gas bulging; formability

1 Introduction

NiAl intermetallic compounds are widely used in the aerospace industry due to their superior physical and chemical properties, such as a high melting point (1638 °C), low density (5.88 g/cm^3), excellent thermal conductivity (76 W/(m·K)), high strength, and oxidation resistance [1−4]. They are expected to serve as next-generation high-temperature structural materials, but their applications face two main barriers: poor toughness and fracture properties at ambient temperature, and poor hot formability [5−7].

Traditionally, NiAl intermetallic compounds are processed using methods such as powder metallurgy, casting, and isothermal extrusion. However, these methods are only suitable for bulk forming and fabricating components with simple shapes and not suitable for forming thin-walled components with complex shapes [8−10]. The traditional methods for manufacturing complex thin-walled components of high-temperature structural materials can be divided into two steps: (1) the sheet preparation with traditional casting – forging − rolling method; (2) secondary forming of the sheets at higher temperatures to obtain the final shape [11,12]. However, NiAl sheets are difficult to prepare due to their intrinsic brittleness and high requirements for the rolling conditions.

In recent years, many researchers have used the foil stacking reaction synthesis (SRS) method and the combined process of accumulative roll bonding and annealing to prepare NiAl intermetallic

Corresponding author: Peng LIN, Tel/Fax: +86-351-6010021, E-mail: linpeng@tyut.edu.cn
DOI: 10.1016/S1003-6326(23)66434-9

compound sheets and other multilayered composites [13−19]. SUN et al [20] used SRS to fabricate NiAl sheets with a homogeneous composition and good performance. The microstructure featured alternately-stacked coarse and fine grain layers that were closely correlated to the thickness of the original foils. The deformation and fracture mechanisms of a synthesized single- phase NiAl sheet with this novel bimodal grain structure were also investigated [21]. FAN et al [22] studied the microstructure and mechanical properties of a NiAl-based composite by a roll bonding and annealing treatment method. The texture of NiAl-based composite sheets is closely related to the initial rolling textures of the original Ni sheets. Although NiAl sheets have been prepared by solid-state synthesis, the forming of NiAl thin-walled components with complex shapes is still a great challenge.

SUN et al [23] developed a novel process that integrated the forming and reaction synthesis to fabricate NiAl alloy curved shells using laminated Ni/Al foils as the initial blanks by stamping with rigid dies. WANG et al [5] put laminated Ni/Al sheets into W-shaped components by stamping using rigid dies. Their results revealed that microcracks generated in the diffused intermediate zone self-repaired through a subsequent reaction. However, this method of rigid die forming is only applicable for forming components with simple shapes and fails when used to form components with complex shapes and closed sections. In addition, to integrate the forming and reaction synthesis, laminated Ni/Al foils need to be under a uniform pressure at every position during the reaction synthesis stage, which cannot be achieved with rigid dies. Therefore, it is desired to prepare more complex thin-walled NiAl components by hot gas bulging.

In addition, Ni/Al micro-laminated composite sheets (NAMCS) can be used to manufacture energetic composite components with good mechanical performance and energy density [24−27]. Therefore, it is important to investigate the formability of Ni/Al micro-laminated composite sheets.

In this study, the microstructure and mechanical properties of NAMCS prepared by the hot pressing of pure Ni/Al foils were investigated. The initiation and propagation of cracks and thickness changes of each layer during tensile deformation at different temperatures were studied to clarify the coordinated deformation mechanism of NAMCS. The fracture mechanism of NAMCS at ambient and high temperatures was also discussed. The formability of NAMCS at 600 °C was evaluated by the limit bulging ratio (ratio of limit bulging height to die diameter), which was tested with the free gas bulging test.

2 Experimental

2.1 Materials preparation

Commercially pure nickel foils (N6) and aluminum foils (1060) with initial thicknesses of 0.06 and 0.09 mm respectively were used to prepare NAMCS. The chemical compositions of the Al and Ni foils are shown in Table 1. To improve the formability of NAMCS, the Ni foils were annealed at 700 °C for 1 h.

The detailed fabrication process of NAMCS was as follows.

(1) Ni and Al foils were cut into 160 mm × 170 mm squares, and the Ni foils were annealed to improve their ductility. Then, they were cleaned with 5 vol.% HF and 15 vol.% NaOH solutions to remove the oxide layers.

(2) The Ni and Al foils were ultrasonically cleaned in 70 vol.% alcohol to remove the residual acid and alkali substances from the surfaces and then dried in a drying oven.

(3) Ni foils (7 pieces) and Al foils (6 pieces) were stacked alternately and then hot-pressed at 630 °C and 20 MPa under a 1×10^{-2} Pa vacuum for 0.5 h to obtain NAMCS with a good interfacial bonding strength. The schematic diagram for the preparation of NAMCS is shown in Fig. 1, and the schematic processing route for preparing NAMCS is shown in Fig. 2.

Table 1 Chemical compositions of Al and Ni foils (wt.%)

Material	Cu	Fe	Mg	Mn	Si	Ti	Za	V	Al	C	S	Ni
Al foil	0.0004	0.015	0.0008	0.0005	0.053	0.016	0.01	0.0005	>99.9			
Ni foil	0.015	0.04	0.01	0.002	0.03					0.01	0.001	>99.9

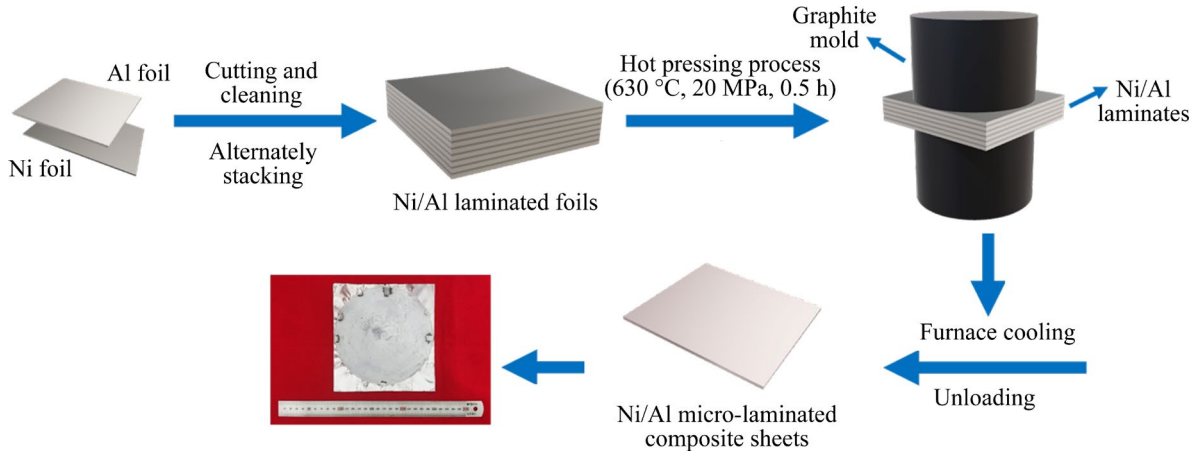

Fig. 1 Schematic diagram for preparation of NAMCS

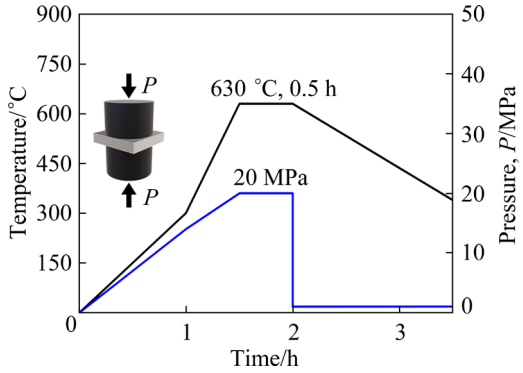

Fig. 2 Schematic processing route for preparation of NAMCS

(4) For comparison with NAMCS, pure Ni and Al laminated sheets with the same total thickness as that of NAMCS were also prepared using the same route in Fig. 2.

2.2 Microstructure characterization

The microstructures of NAMCS and the tensile fracture surfaces were observed with a scanning electron microscope (SEM) equipped with an energy-dispersive X-ray spectrometer (EDS). SEM specimens were prepared by electrochemical polishing in a solution of 6 vol.% perchloric acid, 35 vol.% eugenol, and 59 vol.% carbinol at −30 °C for 30−45 s. The polishing current density and working voltage were set to be 0.6 A/cm^2 and 20 V, respectively. The phase composition of NAMCS was determined using an Empyrean smart X-ray diffractometer (XRD, Philips X'Pert) at 2θ from 15° to 90° with Cu K$_\alpha$ radiation.

2.3 Tensile test

To study the deformation and fracture mechanisms of NAMCS at different temperatures, tensile tests were respectively carried out at room temperature, 300 and 600 °C and an initial strain rate of 1×10^{-3} s^{-1} on a UTM4304 electronic universal testing machine. The tensile specimens with gauge dimensions of 3.5 mm in width and 15 mm in length were cut by electrical discharge machining. Before tests, the samples were mechanically ground and then polished with 0.5 μm diamond suspension. The hold time before tensile deformation was 5 min. Isothermal tensile tests were repeated at least three times to ensure the repeatability of the data. A schematic of the tensile specimen is shown in Fig. 3.

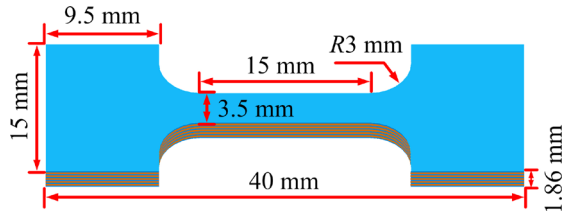

Fig. 3 Schematic diagram of tensile specimen

2.4 Bulging of NAMCS

To investigate the formability of NAMCS, gas bulging tests were carried out, and the ultimate bulging height was measured. Figure 4 shows a schematic diagram and experimental setup of the gas-forming process. The radius of the die bore (r_b) and the die corner (r_c) was 30 and 2.5 mm, respectively. The bulging height was indicated by h. The original and instantaneous thicknesses of the NAMCS during the gas forming were indicated by t_0 and t, respectively. To prevent the sheet from bonding with the die at high temperatures, boron nitride flux was sprayed on both sides of the NAMCS.

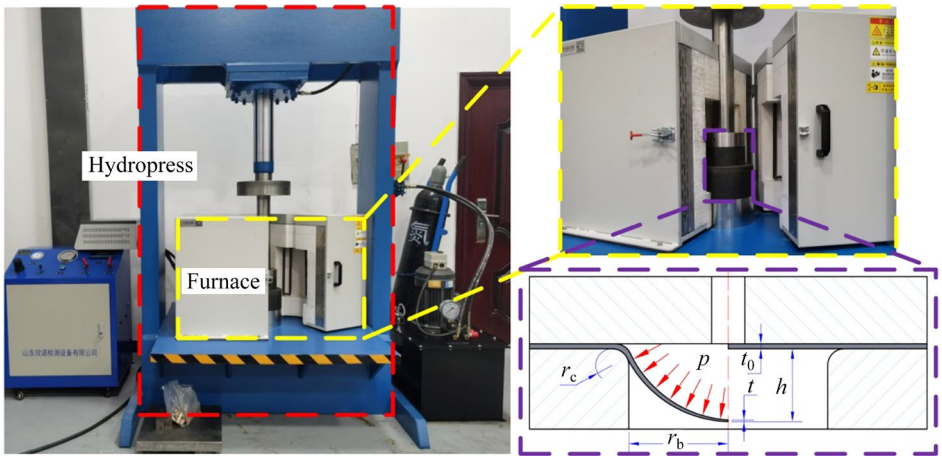

Fig. 4 Schematic diagram and experimental setup of gas-forming process

The gas bulging loading path is shown in Fig. 5. The NAMCS samples were placed in the die and bulged at 600 °C until rupture occurred and then removed from the die. The bugled hemispherical specimens of NAMCS were cut along the bulging height direction, and the wall thickness distribution was measured with a GP−300C measuring microscope.

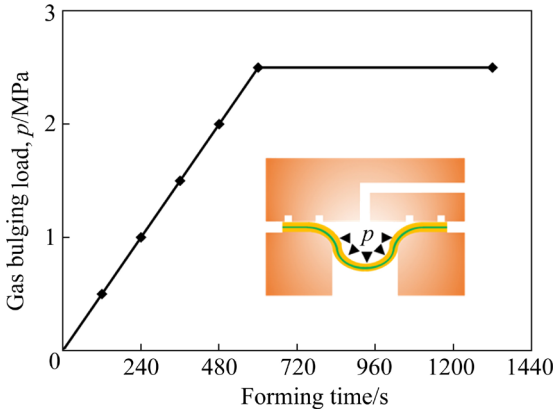

Fig. 5 Gas bulging loading path of NAMCS

3 Results and discussion

3.1 Microstructure of NAMCS

Figure 6 depicts the microstructure of NAMCS samples hot-pressed at 630 °C and 20 MPa for 30 min. The XRD pattern in Fig. 6(c) shows that the phase composition of NAMCS was Al + $NiAl_3$ + Ni_2Al_3 + Ni. The specific compositions of different regions (*A*−*D*) in Fig. 6(b) measured by EDS are recorded in Table 2. In the areas from *A* to *D*, the nickel content gradually increased, while the aluminum content gradually decreased. In Regions *B* and *C*, the molar ratios of Ni to Al were 1:3.0 and 2:3.1, respectively, which were close to the theoretical compositions of the intermetallic compounds $NiAl_3$ and Ni_2Al_3. Thus, the darkest and

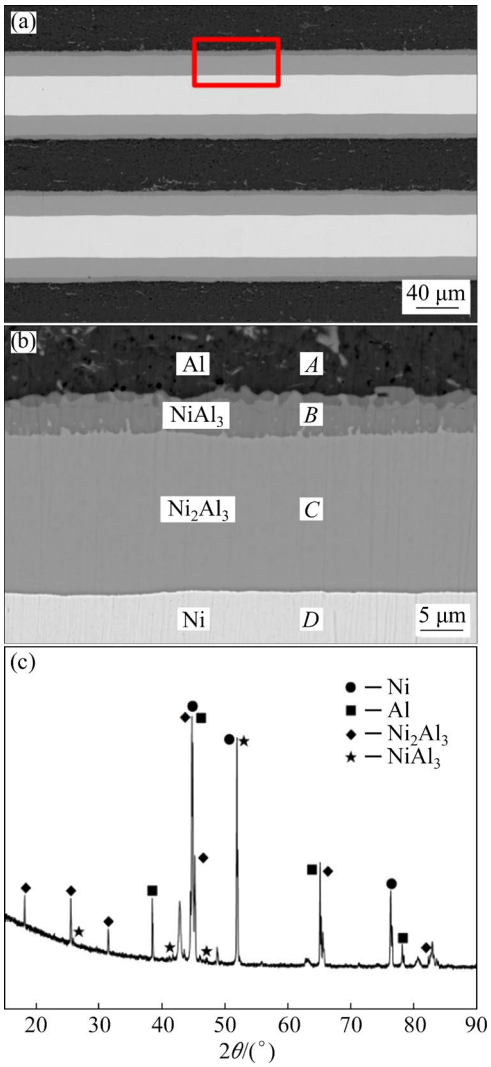

Fig. 6 Microstructures (a, b) and XRD pattern (c) of NAMCS hot-pressed at 630 °C and 20 MPa for 30 min

brightest contrast regions indicated the Al and Ni layers, respectively. The wide gray region with a straight interface on both sides of the Ni layers was a Ni_2Al_3 layer, while the narrow gray region with a rough interface on both sides of the Al layers was the $NiAl_3$ layer.

The average thicknesses of different layers in the Ni/Al system measured by SEM are shown in Table 3. As the diffusion reaction proceeded, the thicknesses of the nickel and aluminum foils gradually decreased, while the thicknesses of $NiAl_3$ and Ni_2Al_3 layers gradually increased. The $NiAl_3$ layer was much thinner than the Ni_2Al_3 layer. The changes in the thickness and phase composition of NAMCS during hot pressing depended on the two-stage diffusion reactions as follows [20]:

$$\text{Step 1: } Ni+3Al \rightarrow NiAl_3+\Delta H_1 \quad (1)$$

$$\text{Step 2: } NiAl_3+Ni \rightarrow Ni_2Al_3+\Delta H_2 \quad (2)$$

In the first stage, the Al layer with a relatively low melting point reacted with the adjacent Ni layer, forming $NiAl_3$ phase grains at the interface. The interface between the $NiAl_3$ and Al layers was the outer grain boundaries of the $NiAl_3$ layers. The waviness was proportional to the $NiAl_3$ grain size. Therefore, the larger grain size of the $NiAl_3$ phase resulted in a rougher interface between $NiAl_3$ and Al layers. In the second stage, the Ni and $NiAl_3$ layers reacted to form Ni_2Al_3 layers.

Table 2 Average compositions in different areas in Fig. 6(b) of NAMCS

Area	Ni content/at.%	Al content/at.%
A	0.75	99.25
B	24.61	75.38
C	39.43	60.56
D	99.37	0.62

Table 3 Average thicknesses of different layers in Ni/Al system measured by SEM

Condition	Thickness/μm			
	Al	$NiAl_3$	Ni_2Al_3	Ni
As-received	90			60
630 °C, 20 MPa, 0.5 h	48.88	5.0	18.61	35.56

3.2 Tensile properties of NAMCS

Figure 7(a) shows the engineering stress−strain curves of NAMCS at room temperature, 300 °C, 600 °C and an initial strain rate of 0.001 s^{-1}. As the temperature increased, the yield strength and ultimate tensile strength of NAMCS decreased, while the elongation did not change monotonically. The sample showed an elongation of 21.5% and an ultimate tensile strength of 175.8 MPa at room temperature. When the temperature increased to 300 °C, the ultimate tensile strength decreased to 117.5 MPa, and the elongation decreased to 18.1%. When the temperature was 600 °C, the elongation increased to 78.7%, while the ultimate tensile strength decreased to 81.1 MPa.

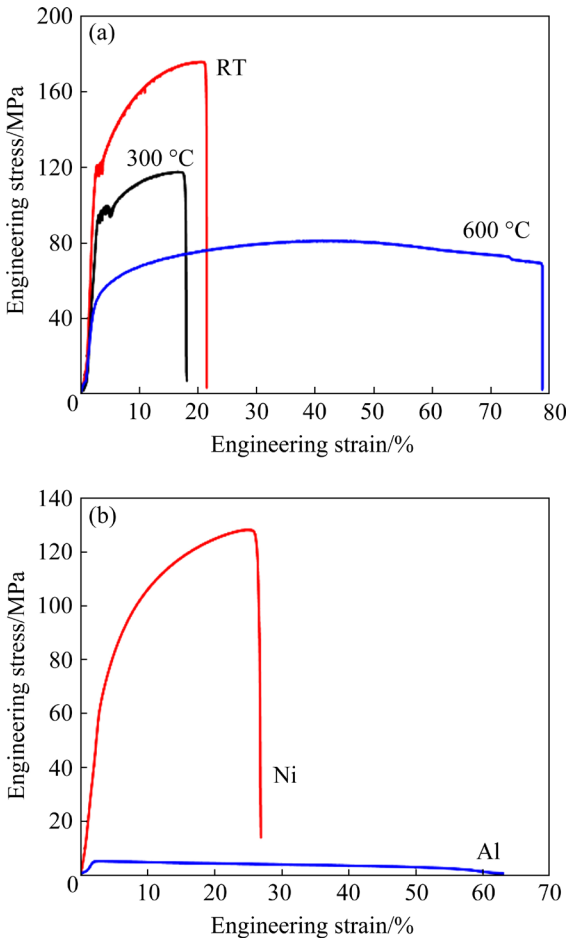

Fig. 7 Tensile engineering stress−strain curves of NAMCS at different temperatures (a), and tensile engineering stress−strain curves of Ni and Al sheets at 600 °C (b)

For comparison, pure Ni and Al sheets were also prepared using the same hot pressing parameters as NAMCS. Figure 7(b) shows the engineering stress−strain curves of pure Ni and Al sheets at 600 °C and a strain rate of 0.001 s^{-1}. Ni sheets exhibited a higher ultimate tensile strength of 128.3 MPa and a much lower elongation of 26.9%.

In contrast, Al sheets exhibited a relatively low ultimate tensile strength of 5.2 MPa and a much higher elongation of 63.0%. The elongation to failure of NAMCS was much higher than that of individual Ni and Al laminates, which was attributed to the improved ductility of $NiAl_3$ and Ni_2Al_3 phases in the laminate structure at 600 °C and the coordinated deformation of Ni_2Al_3 layers with Ni layers.

Figure 8(a) shows the true stress−strain curves of NAMCS at room temperature, 300, and 600 °C. The relationship between the true stress (σ) and true strain (ε) can be described by the Hollomon equation [28]:

$$\sigma=K\varepsilon^n \tag{3}$$

where K is the strength coefficient, and n is the strain-hardening exponent.

To determine n, the natural logarithms of Eq. (3) were calculated as

$$\ln\sigma=\ln K+n\ln\varepsilon \tag{4}$$

The relationship between $\ln\sigma$ and $\ln\varepsilon$ was obtained by substituting the true stresses and the corresponding true strains into Eq. (4), as shown in Fig. 8(b). The slope of the line in Fig. 8(b) represents the value of n. By linear fitting, the values of n at RT, 300, and 600 °C were determined to be 0.29902, 0.24793, and 0.33272, respectively. Generally, n decreased as the temperature increased, and the material with a larger value of n showed a greater tendency to undergo uniform deformation. The value of n reached the minimum at 300 °C, indicating that NAMCS had the lowest ability to undergo uniform deformation. In theory, n should decrease during deformation at 600 °C, but the opposite trend was observed. This was because the Ni_2Al_3 layer with a higher strength was continuously thickened during the deformation, which greatly improved the hardening rate. As the hot pressing time increased, the thickness of Ni_2Al_3 layers within the Ni/Al laminated composite sheet increased, which increased the ultimate tensile strength of the sheet, indicating that the Ni_2Al_3 layer had better high-temperature strength [29]. When the Ni/Al micro-laminated composite sheet deformed at high temperatures, the Ni_2Al_3 layers also thickened. Since it thickened more greatly at 600 °C than at 300 °C, the deformation showed a greater increase with the strain hardening rate at 600 °C.

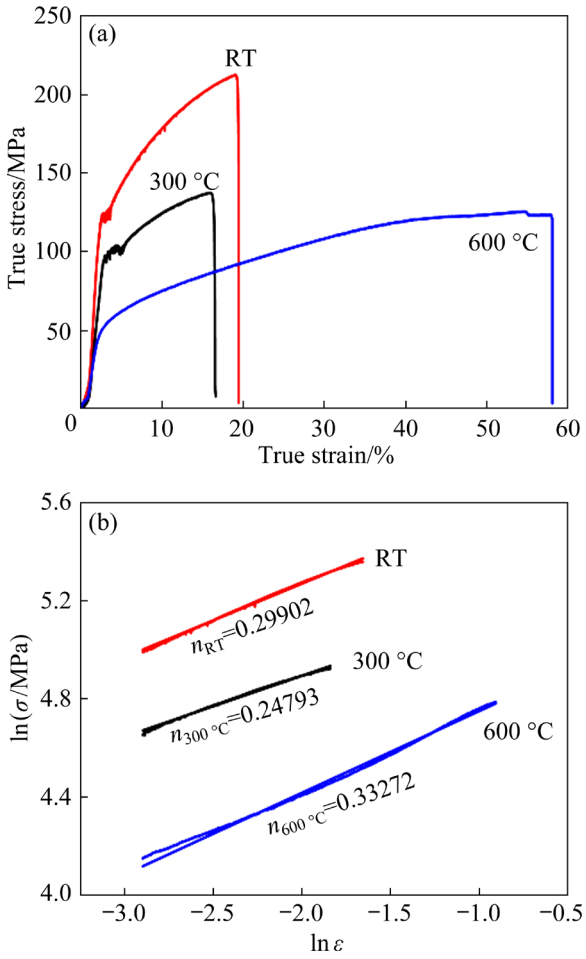

Fig. 8 True stress−strain curves of NAMCS (a), and relationship between $\ln\sigma$ and $\ln\varepsilon$ (b) at different temperatures

3.3 Uniaxial tensile coordinated deformation mechanism of NAMCS

To investigate the uniaxial tensile coordinated deformation mechanism of NAMCS, the microstructure of the samples at different tensile strains was observed, as shown in Fig. 9. At room temperature and 5% strain, some microcracks formed perpendicularly to the loading direction in the $NiAl_3$ and Ni_2Al_3 layers (Fig. 9(a)). However, these cracks did not extend into the Ni and Al layers due to good ductility of Ni and Al. As deformation continued, the width and number of cracks increased, but they never extended to Ni and Al layers until the sample fractured. After deformation, the Ni and Al layers became significantly thinner, as illustrated in Fig. 9(b), indicating that the deformation of NAMCS was dominated by the Ni and Al layers. At 300 °C and 5% strain, narrower and fewer cracks were observed in the $NiAl_3$ and Ni_2Al_3 layers (Fig. 9(c)) compared with those

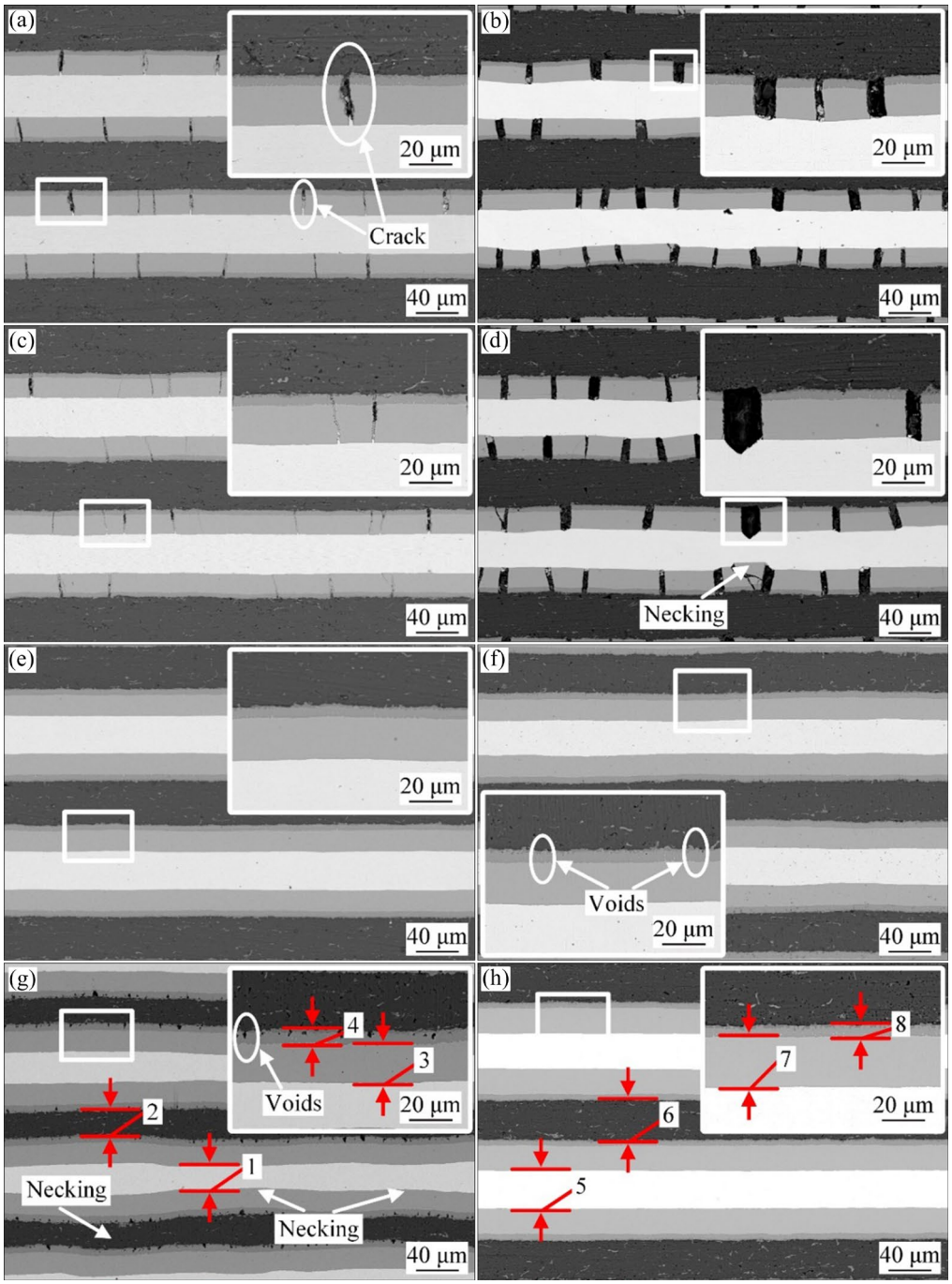

Fig. 9 SEM images of NAMCS at different temperatures and strains: (a) RT, 5%; (b) RT, 18%; (c) 300 °C, 5%; (d) 300 °C, 18%; (e) 600 °C, 10%; (f) 600 °C, 20%; (g) 600 °C, 70%; (h) 600 °C, 0%

deformed at room temperature. This indicated the improved ductility of $NiAl_3$ and Ni_2Al_3 at a higher temperature. When the tensile strain increased to 18%, the width and number of cracks increased, and necking occurred in some locations within Ni and Al layers (Fig. 9(d)). This indicated that, the deformation uniformity, which was heavily dependent on the hardening rate, became worse at higher temperatures. Therefore, increasing the deformation temperature produced two opposing effects on the formability of NAMCS. One was to improve the ductility of $NiAl_3$ and Ni_2Al_3, which improved the elongation to failure. The other was to reduce the hardening rate, which heavily contributed to the deformation uniformity and was prone to decrease the elongation to failure. If the former is dominant, the elongation to failure of NAMCS will increase, while if the latter is

dominant, the elongation to failure of NAMCS will decrease. The deformation of NAMCS at 600 and 300 °C followed the two cases, respectively.

Figure 9(e) showed that the interface of each layer was uniform and smooth without cracks after 10% strain at 600 °C. When the tensile strain increased to 20%, scattered microvoids began to form in the $NiAl_3$ layers, indicating that $NiAl_3$ layers had the lowest ductility (Fig. 9(f)). Due to the huge disparity of $NiAl_3$ to Al in ductility, their deformation was difficult to coordinate well. As a result, cracks formed at the interface between them and finally evolved into microvoids located near the Al layer side in the $NiAl_3$ layers. When the tensile strain increased to 70%, the size and number of voids in the $NiAl_3$ layers increased sharply. No cracks formed in Ni_2Al_3 layers until the sample fractured, indicating good ductility of Ni_2Al_3 layers at 600 °C. Both Ni and Al layers showed various scales of necking, and their thickness decreased obviously, predicting the onset of fracture (Fig. 9(g)). The elongation to failure of pure Ni sheets was only 26.9% at 600 °C, while the Ni layers in NAMCS did not fracture at a tensile strain of 70%. This indicated that the good bonding effect of Ni_2Al_3 to Ni enhanced the plasticity of Ni layers, exhibiting the coordinated deformation of NAMCS.

Table 4 shows the thickness of each layer at different positions of the NAMCS sample after tensile deformation at 600 °C. According to the principle of constant volume, the thickness of each layer should continuously decrease during the deformation. Due to the good ductility and low strength of Ni and Al layers, about a 70% reduction occurred in them, which was nearly consistent with the strain of the whole NAMCS. The Ni_2Al_3 layers were also reduced, further proving their ductility; however, the reduction was less than that of Ni and Al layers due to the simultaneous transformation of Ni and Al into Ni_2Al_3 during deformation. Due to the brittleness of $NiAl_3$ layers, they prematurely cracked without reduction and thickened instead, which was also due to the simultaneous transformation reaction during deformation.

The thickness reduction rate (η) could be calculated by the following equation:

$$\eta=\frac{t_{0\%\ \text{strain}}-t_{70\%\ \text{strain}}}{t_{70\%\ \text{strain}}}\times 100\% \quad (5)$$

where $t_{0\%\ \text{strain}}$ is the NAMCS sample thickness after 0% strain, and $t_{70\%\ \text{strain}}$ is the NAMCS sample thickness after 70% strain.

Table 4 Thickness of each layer at different positions of NAMCS sample after tensile deformation at 600 °C

Strain/%	Thickness/μm			
	Ni	Al	Ni_2Al_3	$NiAl_3$
0	37.70	37.78	24.24	5.45
70	22.22	21.98	18.18	6.06
Thickness reduction rate/%	70	72	33	−10

3.4 Fracture mechanism of NAMCS

Figures 10(a−c) depict the fracture surface of the sample deformed at room temperature. Many dimples, tearing ridges, and ripple patterns can be observed in the Al and Ni layers, implying ductile fracture (Fig. 10(b)). However, the surfaces of the Ni_2Al_3 and $NiAl_3$ layers were relatively smooth and flat, showing remarkable rock candy patterns, implying intergranular fracture (Fig. 10(c)). The different fracture modes of the Al/Ni and Ni_2Al_3/$NiAl_3$ diffusion layers led to uneven fracture surfaces on the samples.

Figures 10(d−f) display the fracture surface of the sample deformed at 300 °C. The fracture surface was flatter than that fractured at ambient temperature. However, there was local separation of the Al layer from the diffusion layer ($NiAl_3$) due to their uncoordinated deformation, which resulted in the lowest elongation to failure for the sample at this temperature, as shown in Fig. 10(d). Many ripple patterns and tearing ridges were found in the Ni and Al layers, suggesting that they still underwent ductile fracture (Fig. 10(e)). The fracture surface of the diffusion layer ($NiAl_3$ and Ni_2Al_3) also showed a rock candy pattern, implying brittle fracture (Fig. 10(f)).

Figures 10(g−i) show the fracture surface of the sample deformed at 600 °C. There was no local separation between the layers, indicating that the diffusion layer was well bonded with the Ni/Al layers. Compared with the other two temperatures, the thinning of the Ni and Al layers was much worse due to drastic plastic deformation (Fig. 10(g)). The thickness of the diffusion layers did not change much, and there were no obvious cracks or holes observed between them, indicating that the Ni and Al layers underwent coordinated deformation with

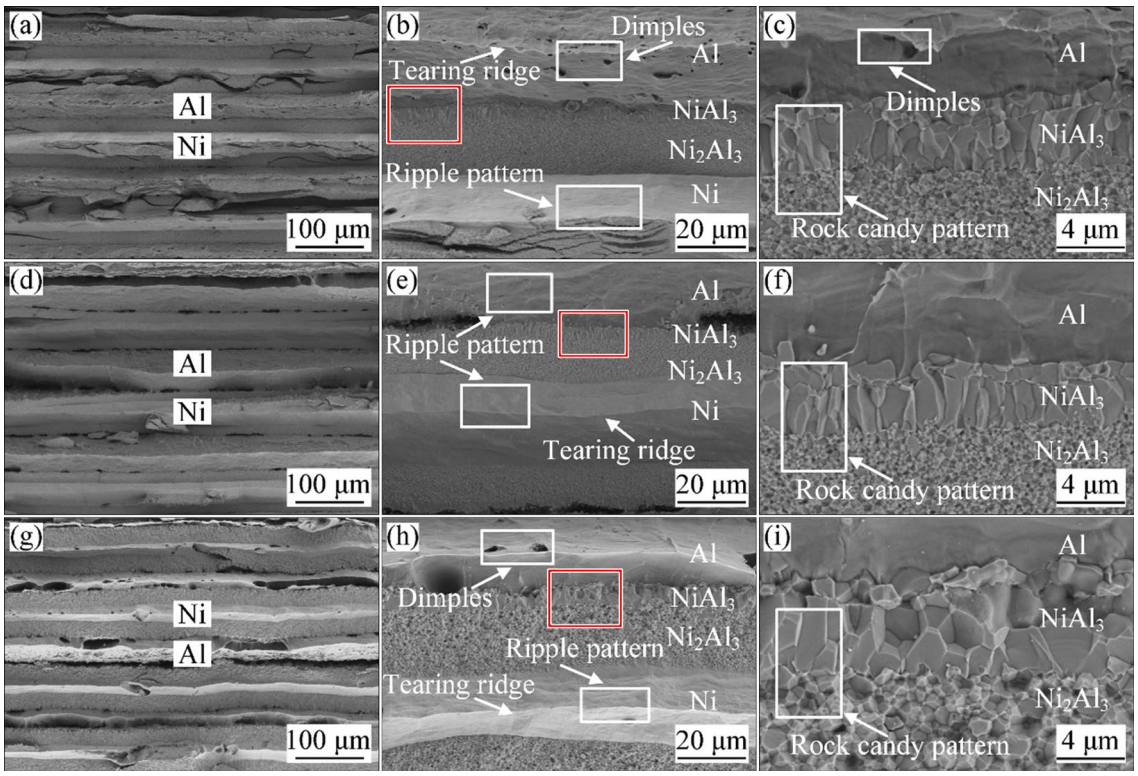

Fig. 10 SEM image showing fracture surface morphologies of NAMCS after tensile tests at different temperatures: (a, b) RT; (c) Magnified SEM image of red box region in (b); (d, e) 300 °C; (f) Magnified SEM image of red box region in (e); (g, h) 600 °C; (i) Magnified SEM image of red box region in (h)

the diffusion layers at this temperature. Furthermore, both Ni and Al layers showed different shapes of dimples, tearing ridges, and ripple patterns, which were typical ductile fracture characteristics. The diffusion layer still exhibited a rock candy pattern and underwent brittle fracture, although the Ni_2Al_3 layers showed good ductility (Figs. 10(h, i)).

3.5 Gas bulging of NAMCS

Due to good ductility of NAMCS at 600 °C and only a few microvoids formed in the $NiAl_3$ layers, the gas bulging temperature was set to be 600 °C. Figure 11 depicts the shells formed from NAMCS, Ni, and Al sheets, which all freely bulged to failure. The cross-section of the NAMCS shell is shown in Fig. 11. Due to different yield strengths between NAMCS, Ni, and Al sheets, the gas bulging pressure and pressure retention time were set to be 2.5, 5, and 0.5 MPa, and 12, 10, and 3 min, respectively. The maximum bulging heights of Ni, Al sheets, and NAMCS were 16, 31, and 20 mm, representing bulging rates of 26.7%, 51.6%, and 33.3%, respectively. The formability of NAMCS was determined by the Ni and Al sheets. Although

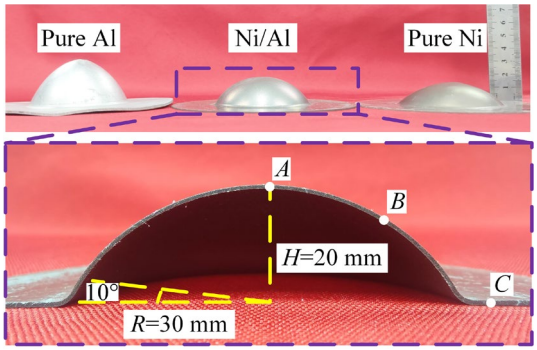

Fig. 11 Gas bulged hemispherical shells of pure Al, pure Ni and NAMCS

the elongation to failure of the Al sheet is lower than that of NAMCS, its bulging rate was higher than that of NAMCS. This was because NAMCS underwent biaxial tensile stress during gas bulging, which more easily caused the crack initiation and propagation in the diffusion layers and reduced the plastic deformation capacity.

The thickness distribution of the NAMCS hemispherical shell from the bottom to top at 10° intervals is shown in Fig. 12. The thinnest point at the top of the hemispherical shell was only

650 μm, representing a thinning rate of 32.29%. The thickness gradually decreased from the bottom to the top due to the depression of the sheet into the inner hole of the die by the gas pressure. According to the principle of constant volume, the deformation of the sheet completely depended on thinning in the thickness direction, i.e., the severer the deformation, the greater the thinning.

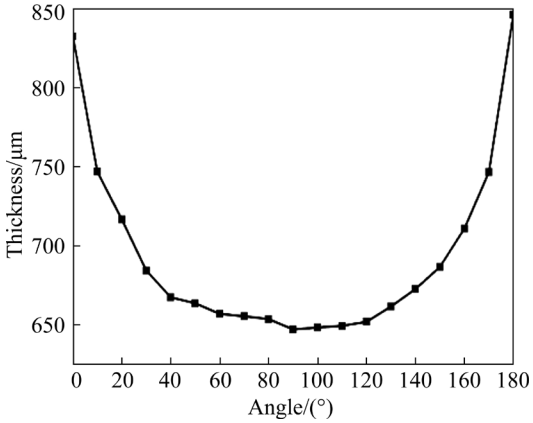

Fig. 12 Thickness distribution of Ni−Al laminated hemispherical shell

Figure 13 presents SEM images of the three typical areas of the NAMCS hemispherical shell shown in Fig. 11. The thickness of each layer at Positions 1–9 in Fig. 13 is listed in Table 5. Point *A* underwent the severest deformation. Local necking occurred on the Ni and Al layers, and the thickness of the Ni_2Al_3 diffusion layers was also reduced. At Point *B*, the thickness reduction of Ni, Al, and Ni_2Al_3 diffusion layers was slightly less than that at Point *A*, but local necking still occurred on Ni and Al layers. It can be detected that Ni_2Al_3 diffusion layers and Ni layers at Points *A* and *B* underwent coordinated deformation. After deformation, although their thickness was greatly reduced, both were still closely bonded, and no cracks were generated. In addition, $NiAl_3$ and Ni_2Al_3 layers were well bonded with irregularly-shaped microvoids on the side of the Al layers, whereas the microvoids did not extend into the Ni_2Al_3 layers. This result was consistent with that of uniaxial tensile deformation. In addition, the maximum reduction rates of Ni and Al layers (about 75%) were almost the same as the elongation to failure of NAMCS. The thickness of $NiAl_3$ and Ni_2Al_3 layers decreased less than the Ni and Al layers, also due to the continued reactive synthesis during heating and hot gas bulging.

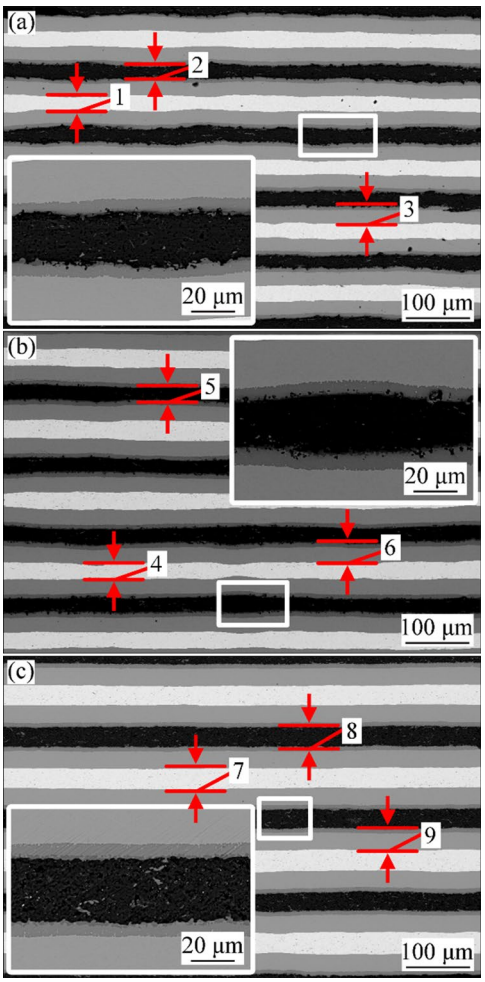

Fig. 13 SEM images of different positions of gas bulged NAMCS spherical shell in Fig. 11: (a) Point *A*; (b) Point *B*; (c) Point *C*

Table 5 Thickness of each layer at different positions of bulged spherical shell

Point in Fig. 11	Thickness/μm		
	Ni	Al	$NiAl_3$+Ni_2Al_3
A	16.66 (1)	14.81 (2)	25.9 (3)
B	18.51 (4)	20.37 (5)	29.62 (6)
C	29.62 (7)	25.92 (8)	37.03 (9)
Thickness reduction rate of Points *A* to *C*/%	78	75	43

Numbers in brackets represent the thickness of Positions 1−9 in Fig. 13

4 Conclusions

(1) The NAMCS sample prepared at 630 °C under 20 MPa for 0.5 h contained four layers (Ni, Al, $NiAl_3$, and Ni_2Al_3) and showed an elongation

of 21.5% and an ultimate tensile strength of 175.8 MPa at room temperature. When the tensile temperature increased from 300 to 600 °C, the ultimate tensile strength decreased from 117.5 to 81.8 MPa, while the elongation to failure increased from 18.1% to 78.7%. The limit bulging ratio of NAMCS at 600 °C reached 33.3%.

(2) Some microcracks perpendicular to the loading direction formed in the $NiAl_3$ and Ni_2Al_3 layers at a tensile strain of 5% from RT to 300 °C, but they did not extend into the Ni or Al layers. At 600 °C and a tensile strain of 20%, some microvoids began to form in the $NiAl_3$ layers, but no cracks formed in the Ni_2Al_3 layers until the sample fractured, indicating a good coordinated deformation ability.

(3) From room temperature to 600 °C, the NAMCS showed identical fracture modes. The fracture mode of the Ni/Al layers was ductile fracture with many ripple patterns, dimples, and tearing ridges, while the fracture mode of the $NiAl_3$ and Ni_2Al_3 diffusion layers was intergranular fracture with rock candy patterns.

CRediT authorship contribution statement

Yu-peng LU: Conceptualization, Writing − Original draft, Methodology; **Hong-liang YIN:** Formal analysis, Methodology, Experiment; **Xian-zheng XI:** Formal analysis, Validation, Investigation; **Ling-jian MENG:** Visualization, Methodology, Review & editing; **Peng LIN:** Resources, Writing − Review draft, Funding acquisition; **Wei LIANG:** Investigation, Formal analysis, Review & editing.

Declaration of competing interest

The authors declare that they have no known competing financial interests or personal relationships that could have appeared to influence the work reported in this paper.

Acknowledgments

This work was supported by the National Natural Science Foundation of China (No. 51505323) and the Applied Basic Research Program of Shanxi Province, China (Nos. 20210302123117, 20210302124658).

References

[1] BOCHENEK K, BASISTA M. Advances in processing of NiAl intermetallic alloys and composites for high temperature aerospace applications [J]. Progress in Aerospace Sciences, 2015, 79: 136−146.

[2] CUI Hong-zhi, WEI Na, ZENG Liang-liang, WANG Xiao-bin, TANG Hua-jie. Microstructure and formation mechanism of Ni−Al intermetallic compounds fabricated by reaction synthesis [J]. Transactions of Nonferrous Metals Society of China, 2013, 23: 1639−1645.

[3] GUNGOR A, DEMIRTAS H. Microstructure and mechanical properties of Fe-doped NiAl−28Cr−6Mo eutectic alloys [J]. Transactions of Nonferrous Metals Society of China, 2016, 26: 1025−1031.

[4] SONG Xiao-jie, CUI Hong-zhi, CAO Li-li, GULYAEV P Y. Microstructure and evolution of (TiB_2+Al_2O_3)/NiAl composites prepared by self-propagation high-temperature synthesis [J]. Transactions of Nonferrous Metals Society of China, 2016, 26: 1878−1884.

[5] WANG Bao, WANG Dong-jun, ZHAO Jie, NING Han-wei, LIU Gang. Deformation behavior and fracture mechanism of a novel laminated Ni/Al sheets during in-situ tensile process [J]. Materials Science and Engineering: A, 2021, 827: 142050.

[6] SHENG Li-yuan, YANG Fang, XI Ting-fei, ZHENG Yu-feng, GUO Jian-ting. Microstructure and room temperature mechanical properties of NiAl−Cr(Mo)−(Hf,Dy) hypo-eutectic alloy prepared by injection casting [J]. Transactions of Nonferrous Metals Society of China, 2013, 23: 983−990.

[7] XU Gui-hua, WANG Guo-feng, ZHANG Kai-feng. Effect of rare earth Y on oxidation behavior of NiAl−Al_2O_3 [J]. Transactions of Nonferrous Metals Society of China, 2011, 21(Suppl.): 362−368.

[8] PALM M, PREUHS J, SAUTHOFF G. Production-scale processing of a new intermetallic NiAl−Ta−Cr alloy for high-temperature application [J]. Journal of Materials Processing Technology, 2003, 136: 105−113.

[9] SKACHKOV O A, POVAROVA K B, DROZDOV A A, MOROZOV A E, POZHAROV S V. Deformation and heat treatment of NiAl−Y_2O_3-based powder alloys: I. Deformation and production of various pressed sections [J]. Russian Metallurgy, 2013(3): 217−219.

[10] SKACHKOV O A, POVAROVA K B, DROZDOV A A, MOROZOV A E, POZHAROV S V, SAMSONOVA M A. Deformation and heat treatment of NiAl−Y_2O_3-based powder alloys: II. fabrication of parts [J]. Russian Metallurgy, 2013(5): 354−356.

[11] MOSLEH A O, KOTOV A D, MEDVEDEVA S V, MIKHAYLOVSKAYA A V. Microstructure evolution of Ti−Al−Mo−V titanium alloy during the superplastic forming with FES estimated strain rates across the formed parts at constant gas pressure [J]. Solid State Phenomena, 2020, 306: 43−52.

[12] LI Xiao, WANG Guo-feng, ZHANG Jing-xuan, LIU Yong-kang. Electrically assisted superplastic forming/ diffusion bonding of the Ti_2AlNb alloy sheet [J]. The International Journal of Advanced Manufacturing Technology, 2020, 106: 77−89.

[13] TURLO V, POLITANO O, BARAS F. Modeling self-sustaining waves of exothermic dissolution in nanometric Ni−Al multilayers [J]. Acta Materialia, 2016, 120: 189−204.

[14] KONIECZNY M. Mechanical properties and deformation behavior of laminated Ni−(Ni_2Al_3+$NiAl_3$) and Ni−(Ni_3Al+ NiAl) composites [J]. Materials Science and Engineering: A, 2013, 586: 11−18.

[15] XI Xian-zheng, LIN Peng, MENG Ling-jian, XUE Shuai-bing, LIN Fei, ZHANG Zhi-xiong, WANG Tao. The

microstructure and mechanical properties of reaction synthesized Ni−Al intermetallic sheets by pure Ni/Al foils with different thickness ratios [J]. Journal of Alloys and Compounds, 2022, 902: 163750.
[16] WANG Q W, FAN G H, GENG L, ZHANG J, CUI X P, PANG J C, QIN S H, DU Y. A novel fabrication route to microlaminated TiB_2−NiAl composite sheet with $\{111\}\langle\mu\nu\omega\rangle$ texture by roll bonding and annealing treatment [J]. Intermetallics, 2013, 37: 46−51.
[17] RAHMATABADI D, PAHLAVANI M, GHOLAMI M D, MARZBANRAD J, HASHEMI R. Production of Al/Mg−Li composite by the accumulative roll bonding process [J]. Journal of Materials Research and Technology, 2020, 9: 7880−7886.
[18] TAYYEBI M, RAHMATABADI D, ADHAMI M, HASHEMI R. Influence of ARB technique on the microstructural, mechanical and fracture properties of the multilayered Al1050/Al5052 composite reinforced by SiC particles [J]. Journal of Materials Research and Technology, 2019, 8: 4287−4301.
[19] SEIFOLLAHZADEH P, ALIZADEH M, ABBASI M R. Strength prediction of multi-layered copper-based composites fabricated by accumulated roll bonding [J]. Transactions of Nonferrous Metals Society of China, 2021, 31: 1729−1739.
[20] SUN Yin, LIN Peng, YUAN Shi-Jian. A novel method for fabricating NiAl alloy sheet components using laminated Ni/Al foils [J]. Materials Science and Engineering: A, 2019, 754: 428−436.
[21] SUN Yin, LIN Peng, YUAN Shi-Jian. Deformation and fracture behavior of the novel NiAl alloy sheet with bimodal laminated structure by in-situ reaction synthesis [J]. Intermetallics, 2020, 127: 106944.
[22] FAN Guo-hua, WANG Qing-wei, GENG Lin, ZHANG Jie, HU Wei-ping, DU Yan. Fabrication, microstructure, and mechanical property of NiAl-based composite with microlaminated architecture by roll bonding and annealing treatment [J]. Metallurgical and Materials Transactions A, 2016, 47: 1280−1291.
[23] SUN Yin, LIN Peng, YUAN Shi-Jian. A novel process for integrated forming and reaction synthesis of NiAl alloy curved shells [J]. Journal of Materials Processing Technology, 2020, 285: 116798.
[24] XIONG Wei, ZHANG Xian-feng, ZHENG Li, BAO Kuo, CHEN Hai-hua, GUAN Zhong-wei. The shock-induced chemical reaction behaviour of Al/Ni composites by cold rolling and powder compaction [J]. Journal of Materials Science, 2019, 54: 6651−6667.
[25] WANG Ming-zhi, QIU Liang-sheng, ZHAO Xing-jian, LI Yuan-zhou, RAO Tian-heng, HE Shi, QIN Liang, TAO Jie. Multilayered Al/Ni energetic structural materials with high energy density and mechanical properties prepared by a facile approach of electrodeposition and hot pressing [J]. Materials Science and Engineering: A, 2019, 757: 23−31.
[26] ZHU Hui-wen, YU Bao-yi, ZHANG Hao, YU Bo-ning, LV Shu-ning, ZHENG Li, LI Run-xia. Effect of annealing treatment on microstructure and mechanical properties of Al/Ni multilayer composites during accumulative roll bonding (ARB) process [J]. Journal of Iron and Steel Research International, 2019, 27: 96−104.
[27] SIMÕES S, VIANA F, RAMOS A S, VIEIRA M T, VIEIRA M F. Anisothermal solid-state reactions of Ni/Al nanometric multilayers [J]. Intermetallics, 2011, 19: 350−356.
[28] HAGGAG F M, WONG H, ALEXANDER D J, NANSTAD R K. The use of field indentation microprobe in measuring mechanical properties of welds [C]//Proceedings of the 2nd International Conference on Recent Trends in Welding Science and Technology. Gatlinburg, Tennessee, USA, 1989: 843−849.
[29] HUANG Zhong-sen. Study on the composite process of internal pressure forming-in-situ reaction synthesis of NiAl alloy thin-walled component [D]. Taiyuan: Taiyuan University of Technology, 2021. (in Chinese)

热压制备 Ni/Al 微叠层复合板的协调变形行为和气压胀形成形性

鲁羽鹏[1]，殷宏亮[1]，席先铮[1]，孟令健[1]，林 鹏[1,2]，梁 伟[1]

1. 太原理工大学 材料科学与工程学院，太原 030024；
2. 太原理工大学 先进金属复合材料成形技术与装备教育部工程研究中心，太原 030024

摘 要：为了制造 NiAl 合金复杂薄壁构件，采用真空热压法制备一种新型 Ni/Al 微叠层复合板(NAMCS)。基于不同温度的单向拉伸试验，研究 Ni/Al 微叠层复合板的力学性能。为了阐明 Ni/Al 微叠层复合板的单向拉伸协调变形机制，通过扫描电子显微镜对不同拉伸应变下的变形组织进行表征。结果表明，在 5%应变、室温和 300 ℃条件下，$NiAl_3$ 层和 Ni_2Al_3 层中形成了一些裂纹。在 600 ℃和 20%应变条件下，在 $NiAl_3$ 层观察到一些微孔。样品在 78.7%的拉伸应变断裂时，Ni_2Al_3 层也未出现裂纹，表现出良好的协调变形能力。Ni/Al 微叠层复合板的高温自由气压胀形试验表明，600 ℃ 时其极限胀形比(极限胀形高度与凹模直径之比)达到 33.3%，表现出良好的成形性。

关键词：Ni/Al 微叠层复合板；力学性能；协调变形机制；气压胀形；成形性

(Edited by Wei-ping CHEN)